

Negative refraction without negative index in metallic photonic crystals

Chiyan Luo, Steven G. Johnson, and J. D. Joannopoulos

*Dept. of Physics and Center for Materials Science and Engineering,
Massachusetts Institute of Technology, Cambridge, MA 02139, USA*

chiyan@mit.edu

J. B. Pendry

*Condensed Matter Theory Group, The Blackett Laboratory, Imperial
College, London SW7 2BZ, United Kingdom*

Abstract: It is shown that certain metallic photonic crystals can enable negative refraction and subwavelength imaging without relying on a negative effective index. These metallic structures are very simple in design and appear straightforward for fabrication. Their unusual electromagnetic response should provide an interesting comparison with the metallic left-handed materials.

© 2003 Optical Society of America

OCIS codes: (160.4670) Optical materials; (230.3990) Microstructure devices; (240.6690) Surface waves

References and links

1. J. B. Pendry, A. J. Holden, W. J. Stewart, and I. Youngs, "Extremely low frequency plasmons in metallic structures," *Phys. Rev. Lett.* **76**, 4773-4776 (1996).
2. J. B. Pendry, A. J. Holden, D. J. Robbins, and W. J. Stewart, "Magnetism from conductors and enhanced nonlinear phenomena," *IEEE Trans. Microwave Theory Tech.* **47**, 2075-2084 (1999).
3. D. R. Smith, W. J. Padilla, D. C. Vier, S. C. Nemat-Nasser, and S. Schultz, "Composite medium with simultaneously negative permeability and permittivity," *Phys. Rev. Lett.* **84**, 4184-4187 (2000).
4. V. G. Veselago, "The electrodynamics of substances with simultaneously negative values of ϵ and μ ," *Sov. Phys. Usp.* **10**, 509-514 (1968).
5. J. B. Pendry, "Negative refraction makes a perfect lens," *Phys. Rev. Lett.* **85**, 3966-3969 (2000).
6. R. A. Shelby, D. R. Smith, and S. Schultz, "Experimental verification of a negative index of refraction," *Science* **292**, 77-79 (2001).
7. D. R. Smith, *Left-handed materials home*, http://physics.ucsd.edu/~drs/left_home.htm
8. E. Yablonovitch, "Inhibited spontaneous emission in solid-state physics and electronics," *Phys. Rev. Lett.* **58**, 2059-2062 (1987).
9. S. John, "Strong localization of photons in certain disordered dielectric superlattices," *Phys. Rev. Lett.* **58**, 2486-2489 (1987).
10. J. D. Joannopoulos, R. D. Meade, and J. N. Winn, *Photonic Crystals: Molding the Flow of Light* (Princeton University Press, Princeton, 1995).
11. H. Kosaka, T. Kawashima, A. Tomita, M. Notomi, T. Tamamura, T. Sato, and S. Kawakami, "Superprism phenomena in photonic crystals," *Phys. Rev. B* **58**, R10096-R10099 (1998).
12. M. Notomi, "Theory of light propagation in strongly modulated photonic crystals: Refractionlike behavior in the vicinity of the photonic band gap," *Phys. Rev. B* **62**, 10696-10705 (2000).
13. C. Luo, S. G. Johnson, J. D. Joannopoulos, and J. B. Pendry, "All-angle negative refraction without negative effective index," *Phys. Rev. B* **65**, 201104-1-201104-4 (2002).
14. C. Luo, S. G. Johnson, and J. D. Joannopoulos, "All-angle negative refraction in a three-dimensionally periodic photonic crystal," *Appl. Phys. Lett.* **81**, 2352-2354 (2002).
15. C. Luo, M. Ibanescu, S. G. Johnson, and J. D. Joannopoulos, "Cerenkov radiation in photonic crystals," *Science* **299**, 368-371 (2003).

16. C. Luo, S. G. Johnson, J. D. Joannopoulos, and J. B. Pendry, "Subwavelength imaging in photonic crystals," submitted to Phys. Rev. B.
17. V. Kuzmiak, A. A. Maradudin, and F. Pincemin, "Photonic band structures of two-dimensional systems containing metallic components," Phys. Rev. B **50**, 16835-16844 (1994).
18. M. M. Sigalas, C. T. Chan, K. M. Ho, and C. M. Soukoulos, "Metallic photonic band-gap materials," Phys. Rev. B **52**, 11744 (1995).
19. E. R. Brown and O. B. McMahon, "Large electromagnetic stop bands in metallodielectric photonic crystals," Appl. Phys. Lett. **67**, 2138-2140 (1995).
20. S. Fan, P. R. Villeneuve, and J. D. Joannopoulos, "Large omnidirectional band gaps in metallodielectric photonic crystals," Phys. Rev. B **54**, 11245-11251 (1996).
21. D. F. Sievenpiper, M. E. Sickmiller, and E. Yablonovitch, "3D wire mesh photonic crystals," Phys. Rev. Lett. **76**, 2480-2483 (1996).
22. K. A. Mcintosh, L. J. Mahoney, K. M. Molvar, O. B. McMahon, S. Verghese, M. Rothschild, and E. R. Brown, "Three-dimensional metallodielectric photonic crystals exhibiting resonant infrared stop bands," Appl. Phys. Lett. **70**, 2937-2939 (1997).
23. K. Sakoda, N. Kawai, T. Ito, A. Chutinan, S. Noda, T. Mitsuyu, and K. Hirao, "Photonic bands of metallic systems. I. Principle of calculation and accuracy," Phys. Rev. B **64**, 045116-1-045116-8 (2001).
24. J. G. Fleming, S. Y. Lin, I. El-Kady, R. Biswas, and K. M. Ho, "All-metallic three-dimensional photonic crystals with a large infrared bandgap," Nature (London) **417**, 52-55 (2002).
25. D. R. Smith, D. Schurig, and J. B. Pendry, "Negative refraction of modulated electromagnetic waves," Appl. Phys. Lett. **81**, 2713-2715 (2002).
26. J. Pacheco, T. M. Grzegorzczuk, B.-I. Wu, Y. Zhang, and J. A. Kong, "Power propagation in homogeneous isotropic frequency-dispersive left-handed media," Phys. Rev. Lett. **89**, 257401-1-257401-4 (2002).
27. S. L. McCall, P. M. Platzman, R. Dalichaouch, D. Smith, and S. Schultz, Phys. Rev. Lett. **67**, 2017-2020 (1991).
28. H. A. Atwater, private communication.

The work of Pendry, Smith, and coworkers [1–3] has given birth to a novel class of metallic structures that has become known as "left-handed metamaterials." These metamaterials are characterized by a negative effective permittivity ϵ and simultaneously a negative effective permeability μ , and can lead to a variety of unusual electromagnetic and optical phenomena [4–6]. For instance, negative refraction of light [4, 6] and subwavelength focusing [5] are two interesting results. Since their discovery, such left-handed metamaterials have received an enormous amount of attention and interest in the scientific community. An up-to-date summary and recent developments in this growing field can be found in [7].

Recently, it has also become clear that dielectric structures with periodic variations on the scale of wavelength, i.e. photonic crystals [8–10], may enable similar anomalous light behavior [11–16]. The physical principles behind these unusual phenomena in photonic crystals are based on complex Bragg scattering effects, and are very different from those in a left-handed metamaterial. For example, both negative refraction and subwavelength imaging may be realized in photonic crystals *without* employing a negative index or a backward-wave effect [13, 16]. Photonic crystals thus represent another class of metamaterial with electromagnetic properties not available in a conventional medium.

This paper aims to extend the concepts of negative refraction and subwavelength focusing without a negative index in dielectric photonic crystals [13, 16] to systems containing metallic components. Such systems, also known as metallic/metallodielectric photonic crystals [17–24], have been studied in detail previously from the viewpoint of forbidden band gaps. Here we focus on the properties of propagating waves in these structures. For simplicity, we consider ideal metals, in which the electric field is everywhere zero without any ohmic losses. Such an ideal metal is the simplest metallic model, is appropriate in the microwave regime, and may also give a useful estimate at infrared frequencies. In contrast to left-handed materials, which currently have two-dimensional

(2D) functionalities but require an intrinsically three-dimensional (3D) analysis, the metallic photonic crystals studied here present a much simpler concept in design: a 2D analysis suffices for all 2D effects, and a 3D crystal can realize truly 3D phenomena. Compared to its all-dielectric counterpart, a metallic photonic crystal also possesses some differences and even advantages in achieving negative refraction. The most significant advantage is that the required refractive index for the crystal constituents can be lowered in a metallic photonic crystal, making negative refraction and subwavelength imaging possible using a broader range of materials. The presence of metals in a photonic crystal may also increase polarization dependence and improve focusing ability, as will be discussed later. For the sake of tractability, throughout this paper we adopt the finite-difference time-domain (FDTD) method as our main computational tool, both to calculate the photonic band structure in the reciprocal space [20, 23] and to perform numerical simulations in the real space.

As in our previous work, we focus on the possibility of all-angle negative refraction (AANR), i.e. a single refracted beam resulting from a single incoming beam at all angles of incidence and traveling on the negative side of the surface normal. This can be realized if a constant-frequency contour near the top region of a photonic band is all-convex and single-branch at a sufficiently low frequency. In contrast to [12], our results are mainly in the first photonic band and are therefore less sensitive to disorder.

We first consider a 2D square lattice (period a) of metallic cylinders immersed in a background medium with dielectric constant $\epsilon = 9$ (e.g. alumina at microwave frequencies). The cylinder radii are chosen to be $r = 0.2a$, corresponding to a modest filling fraction of 13%. In a 2D system, light waves can be classified into TE (electric field in the 2D plane) or TM (electric field parallel to the cylinders) polarizations. The TM polarization is especially interesting for the present metallic system, in which the Bragg scattering effect occurs as if in a dielectric photonic crystal with *infinite* dielectric contrast. In other words, the TM waves now experience the maximum possible artificial spatial modulation in a photonic crystal. We calculate the TM band structure in FDTD by applying Bloch-periodic boundary conditions to a unit cell, and show the results in Fig. 1. The allowed photonic bands start at the frequency $\omega = 0.170(2\pi c/a)$, and there is a Bragg band gap between $0.242(2\pi c/a)$ and $0.280(2\pi c/a)$. Since the first photonic band below the Bragg band gap has a shape similar to that in a dielectric photonic crystal, we can deduce a frequency region for negative refraction from the rounded constant-frequency contours in that band using the approach of [13]. Here, even for the modest filling ratio, the constant-frequency contour in the first band becomes all-convex for frequencies starting at $0.217(2\pi c/a)$ all the way through the band edge $0.242(2\pi c/a)$. As indicated by the inset of Fig. 1, a light beam incident on the (11) (ΓM) surface (the black arrows) will then couple to a single Bloch mode in the crystal (the red arrows). The propagation direction of that Bloch mode, being along the group velocity (i.e. the gradient direction of the constant-frequency contours), is on the negative side of the surface normal, giving rise to negative refraction. Furthermore, the phase-space region of air spanned by all the propagating waves and projected on the (11) direction can be matched in size to that of the photonic crystal, enabling AANR. This is also indicated in a frequency range in Fig. 1. The existence of AANR is the starting point for superlensing in photonic crystals [13, 16]. We note that a negative refraction effect also exists in a crystal made of the same metallic cylinders in air instead of in a background dielectric. However, the photon frequencies of the metal-in-air case increase by a factor of $\sqrt{\epsilon} = 3$, making the air phase space much larger than that of the crystal and thus destroying AANR.

We proceed with a computational experiment of negative refraction in the present photonic crystal. Here, a continuous-wave (CW) Gaussian beam of frequency $\omega_0 =$

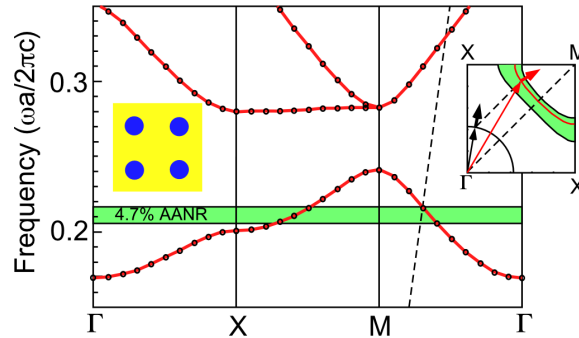


Fig. 1. The first few bands of a 2D square lattice of metallic cylinders in dielectric computed by FDTD. The photonic dispersion relations are indicated by black circles and connected by red lines. The broken line is the light line centered on the M point. The green AANR region is the frequency range of negative refraction for all incident angles. The left inset is a schematic illustration of the photonic crystal (yellow stands for dielectric and blue stands for metal). The right inset is a portrayal of the Brillouin zone and the refraction in wavevector space. Air modes and photonic-crystal modes are indicated by black and red colors, respectively. The long and thin arrows indicate the phase velocity \mathbf{k} , and the short and thick arrows indicate the group (energy) velocity $\partial\omega/\partial\mathbf{k}$. The green region is the phase space corresponding to the AANR frequency range.

$0.216(2\pi c/a)$ and a half width $\sigma = 5.8\lambda_0$ ($\lambda_0 = 2\pi c/\omega_0$) is launched at 45° incidence toward the (11) surface and subsequently reflects away from and refracts into the metallic photonic crystal. In the computation, we use a finite crystal and impose perfectly matched layer (PML) boundary regions. Figure 2 shows a snapshot of this refraction process. It can be clearly seen that the overall electromagnetic energy in the metallic photonic crystal travels on the “wrong” side of the surface normal. The refraction angle is about -12° , consistent with results from the wavevector space. If we look closely at the refracted field profile in the photonic crystal, we can see that the constant-phase locations lie on parallel straight lines and form “phase fronts” in the photonic crystal. However, since the constant-phase regions in the crystal are located in discrete cells and separated from each other, there exist multiple ways to connect them and hence multiple choices of phase-front definition (Fig. 2, inset). This reflects the fact that, in a photonic crystal, \mathbf{k} is only defined up to a reciprocal lattice vector \mathbf{G} . Here, we define the phase fronts for the refracted beam to be the set of constant-phase lines with the largest wavelength, which corresponds the smallest $|\mathbf{k}|$ and hence the unique \mathbf{k} in the first Brillouin zone. We then choose the gradient direction to this set to be the direction of the phase-front normal. These refracted phase fronts gradually move into the crystal as time progresses and their normal points toward the *positive* side of the surface normal. This phenomenon is naturally explained by the inset of Fig. 1 which shows that \mathbf{k} experiences positive refraction while $\partial\omega/\partial\mathbf{k}$ goes negative. It also explains the different physics of the present negative refraction as compared to that in the left-handed materials: here negative refraction is realized in the first photonic band that consists of forward-propagating waves ($\mathbf{k} \cdot \partial\omega/\partial\mathbf{k} > 0$), not backward-propagating waves as in a left-handed material. The present effect bears certain similarity to the negative refraction of energy and positive refraction of *modulation interference fronts*, pointed out recently in left-handed materials [25, 26]. However, it is important to note that in our simulation only a CW wave of a single frequency is used and the phase fronts studied here are not the modulation interference fronts, which must be made from multiple frequencies.

We have calculated the TM AANR frequency range for several other values of cylin-

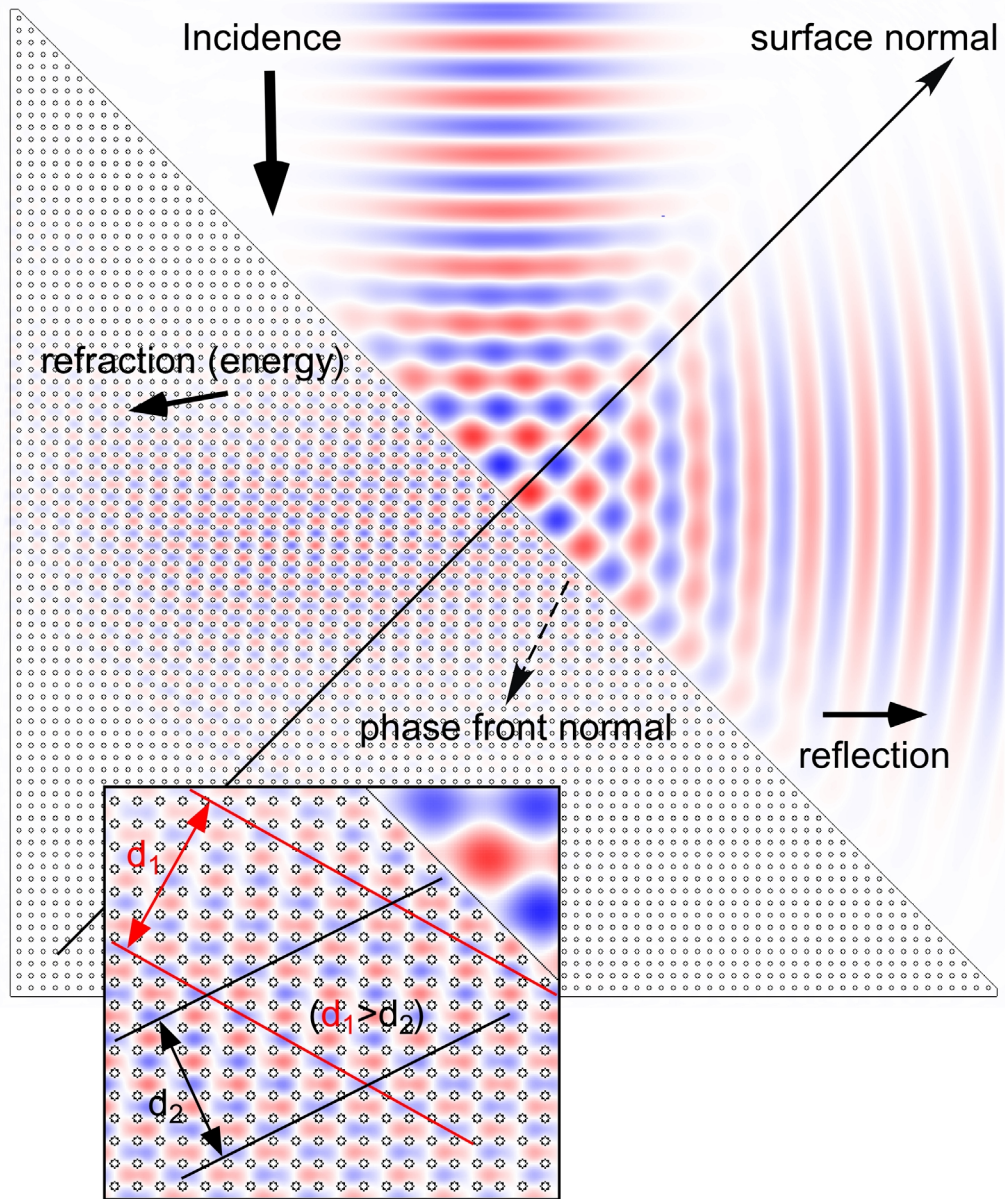


Fig. 2. FDTD simulation of negative refraction. Shown is the pattern for the electric field \mathbf{E} perpendicular to the plane (red for positive and blue for negative values). The dielectric and metallic boundaries are in black. The arrows and texts illustrate the various beam directions. The inset shows two possible ways of constructing phase fronts from the field pattern. We choose the set of phase fronts with the maximum wavelength distance (a maximum 4-wavelength distance d_1 of that set is shown in red) to be the phase fronts of the refracted beam.

der radii, and the results are given in Table 1. The AANR frequency range is between ω_l and ω_u , and the M edge of the first band is also listed for reference. The data show a steady increase of all frequencies with cylinder radii. For $r/a > 0.3$, the TM bands in metallic photonic crystals have very narrow bandwidths and thus small AANR ranges. These TM modes in 2D can be easily realized by sandwiching a finite-height 2D crystal between parallel metallic plates [27]. We have also computed the AANR frequencies in the first band for the TE polarization, which do not show large shifts with the cylinder sizes (below $0.25(2\pi c/a)$ for all r). In the TE case the metallic photonic crystals behave in a manner very similar to an air-in-dielectric all-dielectric crystal, in which large filling ratio ($r/a > 0.3$) is typically preferred in achieving TE AANR. Thus, a 2D metallic photonic crystal with large cylinders can allow AANR for the TE polarization but exhibit complete reflection for TM waves of the same frequency. These results can be compared to those in all-dielectric photonic crystals, where there exists less distinction in whether AANR exists between the TE and TM polarizations [13].

Let us turn to 3D periodic systems. We have calculated a body-centered cubic (BCC) lattice of nonoverlapping metallic spheres in a background dielectric, and found that AANR in full 3D can be accomplished near the frequency $\omega = 0.385(2\pi c/a)$ for a modest background permittivity of $\epsilon = 3$ and a sphere diameter of $0.85a$, a being the side length of the conventional cubic cell of the BCC lattice. This situation is analogous to our recent work on a 3D dielectric photonic crystal [14]. It is worth noting that this 3D metallodielectric crystal has very important advantages over an all-dielectric structure in achieving AANR: the index requirement for the background matrix is quite low and can be satisfied for many materials, and straightforward fabrication procedures are available at present [19]. All these results are readily amenable to experimental verification, and the advantages of metallic photonic crystals should make them a very attractive structure for studies of 3D negative refraction.

Table 1. AANR frequency range for various cylinder radii (TM polarization)

Cylinder radii (r/a)	lower limit ($\omega_l a/2\pi c$)	upper limit ($\omega_u a/2\pi c$)	band edge at M ($\omega_M a/2\pi c$)
0.10	0.195	0.196	0.236
0.15	0.196	0.205	0.238
0.20	0.207	0.217	0.242
0.25	0.231	0.238	0.255
0.30	0.257	0.261	0.271

We now examine the subwavelength imaging effect of a planar slab, one of the most striking consequences for negative refraction. This effect was first proposed in the context of left-handed materials [5], and recently it has been shown that a slab of AANR dielectric photonic crystal is able to focus a point source into a point-like image with a width below the diffraction limit [13]. With the AANR frequencies for our metallic photonic crystals identified above, it is possible to investigate their subwavelength imaging properties in a similar manner by considering evanescent waves coupling to the bound states of the slab. Note that amplification of one evanescent wave alone is independent of negative refraction and can be done using metallic surface plasmons [28].

Below, we focus on a 2D metallic photonic crystal for simplicity. Here, the bound-photon band structure of a photonic-crystal slab finite in thickness but infinite in the transverse direction is of interest. We place the slab in the center of a computational supercell that is exactly one surface-period wide along the transverse direction and a few times longer than the slab thickness h in the (11) normal direction. The boundary

conditions of the computational cell are Bloch-periodic on the transverse sides with PML regions on the normal sides. The bound photon states computed in this way for the crystal in Fig. 1 are plotted in Fig. 3. As shown in Fig. 3, when h changes from $5.9a$ to $6.0a$, relatively little variation occurs in the bulk-guided modes, but the frequencies of the surface mode sweep through the AANR frequency range. Moreover, flat portions exist in both the surface and the bulk bound states at common frequencies covering the range of wavevectors outside the light cone. These bound states are the poles of transmission for evanescent waves, and consequently they can be used to amplify incident evanescent waves, i.e. to transfer a range of near fields on one side of the slab to the other side. In this way, images formed by AANR can be further focused to subwavelength resolutions.

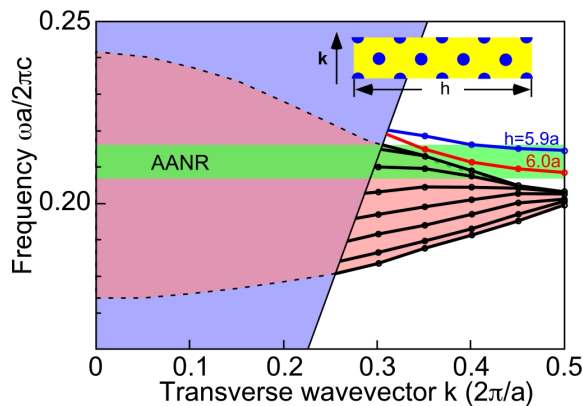


Fig. 3. Bound photon modes inside a slab of metallic photonic crystal plotted on top of the projected surface band structure. The black circles and lines indicate the bulk-guided modes. The colored circles and lines represent the surface-guided modes for two different slab thicknesses. The lightly red region is the bulk band structure projected to the surface direction, and the lightly blue region is the light cone. Inset is a schematic illustrations of the photonic-crystals slab of finite thickness h .

We perform FDTD simulations with PML boundary conditions for subwavelength focusing using a metallic-photonic-crystal slab of thickness $6.0a$. The results are summarized in Fig. 4, which shows time-averaged intensity ($|\mathbf{E}|^2$) distributions of two slightly different frequencies close to that of the flat bound photon bands in Fig. 3. The two frequencies illustrate the delicate interplay between the propagating and evanescent waves in image formation. For $\omega = 0.2120(2\pi c/a)$, an isolated intensity maximum with width about 0.67λ can be realized in the image space $z > 0$ if the evanescent waves are amplified to values comparable with those of the propagating waves. However, because of the resonant nature of the present situation (no loss is assumed) and the extremely small group velocities of the bound photon modes, some transmitted evanescent waves can also have such an extraordinarily enhanced amplitude that they dominate over other evanescent and all propagating waves. This leads to the enhanced resonance effect at $\omega = 0.2116(2\pi c/a)$, for which large field oscillations exist in both the bulk crystal and the surfaces, and the transverse image profile becomes delocalized and is no longer an isolated peak. Both scenarios here demonstrate the amplification effect of evanescent waves across the photonic-crystal slab. Moreover, the situation in which the propagating and evanescent waves are balanced, i.e. $\omega = 0.212(2\pi c/a)$ in this example, is particularly interesting because it illustrates the focusing of evanescent waves and the subwavelength imaging capacity of the metallic photonic crystal. In the present case, the discreteness of the computational grid limits our tuning capacity for bound photon states, but in an ideal situation, with a suitably tuned photonic-crystal surface struc-

ture where the bound photon bands are sufficiently flat and all evanescent waves inside the first Brillouin zone are amplified, the full imaging width will only be limited by the surface periodicity and not by the wavelength of light. A distinctive feature for the metallic photonic crystal studied here is that, since fields cannot enter the ideal metal, the spatial variation of near-field waves can be stronger than in the dielectric photonic-crystal case. For example, the intensity is always zero near the metallic components on the surface, and a strong intensity maximum along z axis *always* exists in the image space, even in the limit of extremely large evanescent wave strengths near the surface. This effect creates a very localized and intense optical focus in free space and might be useful in realistic applications.

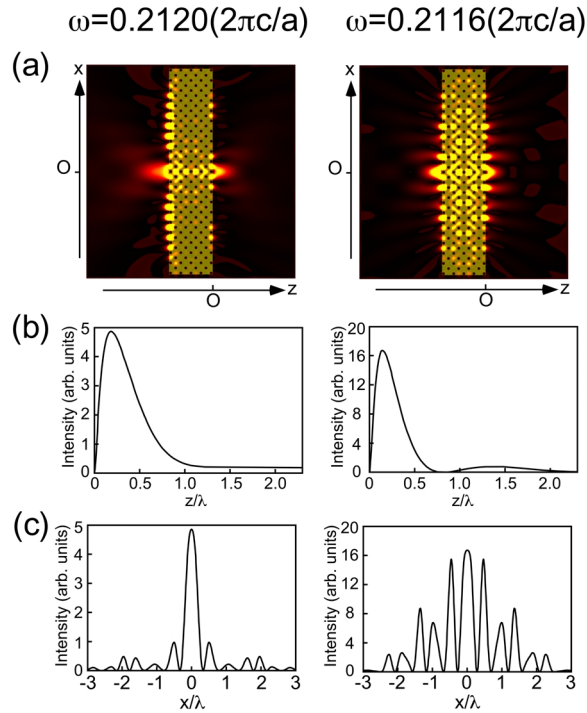


Fig. 4. FDTD simulation of superlensing with metallic photonic crystal. Each column correspond to the results for a CW point source placed at $0.207a$ away from the left surface of the slab, for the frequency value indicated at the top. (a): Intensity distribution in the system marked with the directions of coordinate axes x and z . The intensity is calculated as the averaged square of the electric field value between 2174 and 2416 periods. A lighter color represents a higher intensity value. The point source is placed at $(z, x) = (-6.21a, 0)$. (b): Intensity distribution data plotted along the surface direction in the image space ($x = 0, z > 0$). (c): Intensity distribution data measured at the z value of the intensity peak in (b), plotted along the transverse direction (x).

The numerical calculations in this paper are carried out for ideal systems with monochromatic sources and lossless metals. These CW results can also be applied to situations with finite pulses, as long as the pulse bandwidth is sufficiently narrow. An estimate for the upper limit of the pulse bandwidth at which negative refraction is still observable is 4%–5%, i.e. the frequency range of AANR. For subwavelength imaging, which relies on flat bound photon bands with a strong group-velocity dispersion, the required bandwidth is narrower and should be smaller than roughly 0.2%, corresponding to the frequency difference in Fig. 4. For small absorption losses in metals, their qualitative effect is to introduce a finite decay length to propagating waves in the crystal,

and negative refraction can be observed as long as this decay length exceeds the sample dimensions. For evanescent waves, losses bring a finite lifetime to the bound photon modes and reduce the magnitude of the associated near-field amplification. Provided that these loss-induced modifications are also small for wavevectors inside a finite region outside the light cone in Fig. 3, the focusing effect of planar slabs would continue to be subwavelength. All of these requirements can be easily satisfied in the microwave regime, suggesting that both AANR and subwavelength imaging in metallic photonic crystals are amenable to experimental studies. In another work pending publication [16], we investigated the quantitative effects of absorption losses in all-dielectric photonic-crystal superlenses, and found that a subwavelength focusing full-width of $\sim 0.5\lambda$ may be achieved using materials with a loss tangent of $\sim 10^{-4}$.

In conclusion, we have demonstrated that metallic structures can also be designed in a simple way to realize both negative refraction and subwavelength imaging without relying on the concept of a left-handed material. These metallic designs can offer specific characteristics and realistic advantages as compared to their all-dielectric counterparts. The present work represents an alternative method of achieving unusual optical phenomena using deliberately designed metallic structures.

Acknowledgments

This work was supported in part by the NSF's MRSEC program under Award No. DMR-9400334 and the DoD/ONR MURI Grant No. N00014-01-1-0803.